












RESEARCH ARTICLE | APRIL 17 2024

## Precisely tunable and predictable index-near-zero modes across continuous and broad bands

Panpan He ; Yun Shen ; Sanshui Xiao ; Lujun Hong ; Yun You ; Kosmas L. Tsakmakidis  ; Yamei Luo  ; Jie Xu  



*Appl. Phys. Lett.* 124, 161109 (2024)

<https://doi.org/10.1063/5.0209239>



View  
Online



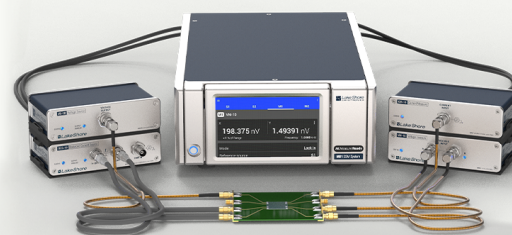
Export  
Citation



### An innovative I-V characterization system for next-gen semiconductor R&D

Unique combination of ultra-low noise sourcing + high-sensitivity lock-in measuring capabilities

[Learn more](#)



# Precisely tunable and predictable index-near-zero modes across continuous and broad bands

Cite as: Appl. Phys. Lett. **124**, 161109 (2024); doi: [10.1063/5.0209239](https://doi.org/10.1063/5.0209239)

Submitted: 19 March 2024 · Accepted: 3 April 2024 ·

Published Online: 17 April 2024



View Online



Export Citation



CrossMark

Panpan He,<sup>1,2</sup> Yun Shen,<sup>3</sup> Sanshui Xiao,<sup>4</sup> Lujun Hong,<sup>3</sup> Yun You,<sup>5</sup> Kosmas L. Tsakmakidis,<sup>6,a)</sup>   
Yamei Luo,<sup>7,a)</sup> and Jie Xu<sup>7,a)</sup>

## AFFILIATIONS

<sup>1</sup>College of Electrical and Electronic Engineering, Luzhou Vocational and Technical College, Luzhou 646000, China

<sup>2</sup>Luzhou Key Laboratory of Intelligent Control and Applications Technology of Electronic Devices, Luzhou Vocational and Technical College, Luzhou 646000, China

<sup>3</sup>Institute of Space Science and Technology, Nanchang University, Nanchang 330031, China

<sup>4</sup>DTU Fotonik, Department of Photonics Engineering, Technical University of Denmark, DK-2800 Kgs. Lyngby, Denmark

<sup>5</sup>School of Science, East China JiaoTong University, Nanchang 330013, China

<sup>6</sup>Section of Condensed Matter Physics, Department of Physics, National and Kapodistrian University of Athens, Panepistimioupolis, Athens GR-157 84, Greece

<sup>7</sup>School of Medical Information and Engineering, Southwest Medical University, Luzhou 646000, China

<sup>a)</sup>Authors to whom correspondence should be addressed: [ktsakmakidis@phys.uoa.gr](mailto:ktsakmakidis@phys.uoa.gr); [luoluoyan@126.com](mailto:luoluoyan@126.com); and [xujie011451@163.com](mailto:xujie011451@163.com)

## ABSTRACT

In the past two decades, index-near-zero (INZ) modes and materials, with their spatial phase invariance and super coupling, gained increasing attention for applications in all-optical/quantum computing and communication. However, the modulation of INZ modes is typically complex and discontinuous, often achieved through intricate experimental methods, thereby hindering their widespread application. Here, we propose two deep-subwavelength magneto-optical one-way waveguides and discover three broadband tunable INZ modes, exhibiting predictable behavior dependent on the external magnetic field (EMF). By utilizing these INZ modes, we design broadband tunable all-optical phase modulators through straightforward EMF control. The tunable and predictable nature of INZ modes, combined with deep-subwavelength phase modulators, may advance miniaturized all-optical communication and computation.

© 2024 Author(s). All article content, except where otherwise noted, is licensed under a Creative Commons Attribution (CC BY) license (<https://creativecommons.org/licenses/by/4.0/>). <https://doi.org/10.1063/5.0209239>

Given the impending global energy crisis, the imperative to substitute inefficient energy sources with sustainable and cleaner alternatives, such as nuclear energy, is crucial. Furthermore, utilizing low-loss and high-speed light/photon or electromagnetic (EM) waves for signaling communication and computation, rather than electronic/electrical energy, presents a viable solution. The challenge is to manipulate EM waves in a simple yet efficient manner. Achieving zero-phase-shift transmission and/or communication of EM waves would significantly facilitate their manipulation. In this context, the index-near-zero (INZ) mode has been proposed and extensively studied.<sup>1,2</sup>

Specifically, the INZ mode can be classified into three categories: the  $\epsilon$ -near-zero (ENZ) mode with near-zero (effective) permittivity,<sup>3</sup> the  $\mu$ -near-zero (MNZ) mode with near-zero (effective) permeability,<sup>4,5</sup> and the  $\epsilon$ -and- $\mu$ -near-zero (EMNZ) mode with both (effective) permittivity

and (effective) permeability near zero.<sup>6,7</sup> INZ modes can be realized in various systems, including waveguides near cutoff,<sup>2,8,9</sup> layered structures based on effective medium theory,<sup>10,11</sup> resonant cavities via resonant tunneling,<sup>12</sup> and photonic crystals (PhCs) with Dirac-cone dispersion.<sup>13–16</sup> Despite significant progress in INZ-related theory and manufacturing techniques, there remain limitations, such as prohibitive fabrication costs and complex processes,<sup>17</sup> discontinuous operating frequencies, relatively large device heights, and loss.<sup>15</sup> Finding an additional platform to flexibly tune the INZ mode across a wide range and render it insensitive to fabrication imperfections remains a challenge.

Magneto-optical (MO) one-way waveguides/modes have gained increasing attention in recent years due to their unique magnetically controllable properties.<sup>18–20</sup> Similar to topologically protected boundary modes, MO one-way modes exhibit excellent “collimation” along

the waveguide/surface.<sup>21,22</sup> These modes can be broadly categorized into two groups: PhCs made of MO materials and straight heterostructures consisting of continuous MO materials. In both cases, an external magnetic field (EMF) is applied to break the time-reversal symmetry of the system, resulting in one-way propagation. MO one-way modes have been utilized in various optically functional devices, such as filters<sup>23</sup> and splitters.<sup>24</sup>

Recently, “theoretically tunable” INZ modes were achieved using one-way magneto-optical (MO) waveguides.<sup>25</sup> The modulation of the INZ mode solely relied on adjusting the waveguide thickness parameters, presenting practical challenges. In this study, we demonstrate that by designing appropriate EMFs, two types of one-way MO waveguides can realize tunable INZ modes across a wide range, with the bandwidth contingent upon EMF alterations. We identify several predictable INZ modes in these structures, each with a specific frequency-EMF relationship. Remarkably, we achieve broadband phase modulators with a  $2\pi$  phase shift ( $-\pi \leftrightarrow \pi$ ) relying on these tunable and predictable one-way INZ modes. We assess the loss effect and robustness of the INZ modes through numerical simulations using the finite element method (FEM).

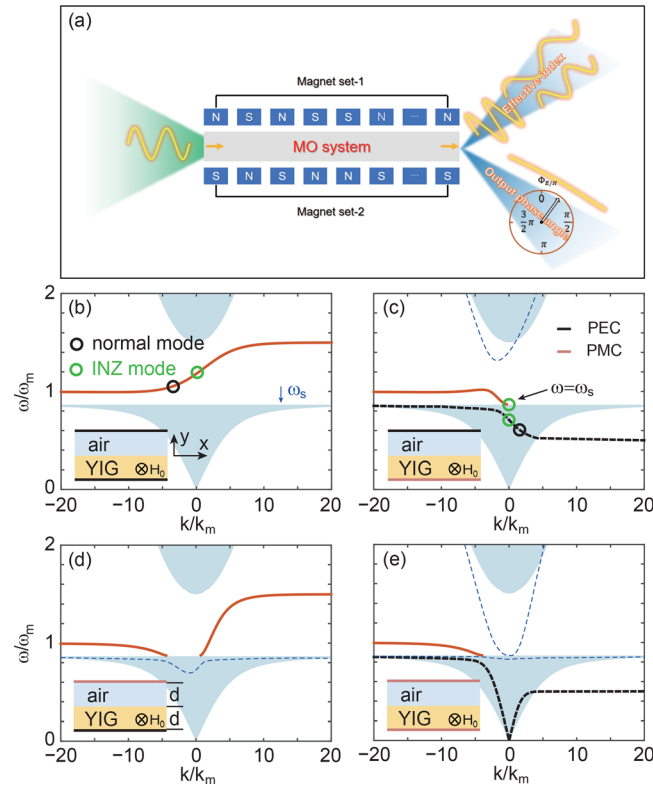


**FIG. 1.** (a) The schematic of adjusting the effective index and/or phase angle of the output wave. (b)–(e) Dispersion diagrams for (b) type-1, (c) type-2, (d) type-3, and (e) type-4 one-way waveguides as the thicknesses of the air and YIG layers being the same and  $d = 0.03\lambda_m$  ( $\lambda_m = 2\pi c/\omega_m$ ). The green and black circles in (b)–(c) represent the INZ modes and normal modes within the one-way regions, respectively. The red and black lines represent surface modes in the respective structures. The shaded areas indicate the bulk zones of an infinite YIG layer, while the blue dashed line represents compressed bulk modes in finite YIG layers in all four structures. The other parameters used in the diagrams are  $\epsilon_r = 1$  (for air) and  $\omega_0 = 0.5\omega_m$  (for YIG).

MO waveguides offer the advantage of adjusting performance and functionalities via EMF modifications. Here, we propose that by carefully engineering the EMF [as illustrated in Fig. 1(a)], an MO system/waveguide can effectively tune the output wave’s effective index from near zero to infinity. Moreover, as the operating frequency approaches the INZ frequency ( $\omega_{\text{INZ}}$ ) of the waveguide, the output phase angle can be tuned across a complete  $2\pi$  range. These tunable effective index and/or output phase angle characteristics hold significant promise for applications in optical communication and computing.

Achieving a wide range of effective index values while keeping the frequency consistent necessitates tunability of the wavenumber from near zero (INZ wave) to infinity. Through theoretical analysis, we identify two types of microwave waveguides capable of achieving this objective. The first type of one-way structures (type-1) was designed for trapping magnetic rainbows.<sup>26</sup> As depicted in the inset of Fig. 1(b), the type-1 structure is bounded by perfect electric conductor (PEC) walls in the longitudinal direction. The second waveguide is akin to the type-1 waveguide but features a lower boundary replaced by a PMC wall [see Fig. 1(c)]. Although PMC is not a naturally occurring material, high-impedance surfaces (HIS) have been demonstrated as an effective means to create PMC or quasi-PMC in the microwave<sup>13,27</sup> and terahertz<sup>28</sup> regimes.

To investigate the impact of a PMC boundary on the performance of an MO one-way waveguide, we analyzed four different waveguide structures. The first two structures comprised the type-1 and type-2 one-way waveguides, while the remaining two structures acted as reference structures. Specifically, the type-3 one-way waveguide featured a PMC boundary on the upper side and a PEC wall on the lower side [see the inset of Fig. 1(d)]. The type-4 one-way waveguide was bounded by two PMC walls [demonstrated in Fig. 1(e)]. The dispersion equations for these one-way waveguides are given by the following equation:

$$\begin{cases} \frac{\alpha}{\tanh(\alpha d)} + \frac{\mu_2}{\mu_1} k + \frac{\alpha_d \mu_v}{\tanh(\alpha_d d)} = 0, & (\text{type-1}), \\ \alpha \cdot \frac{\tanh(\alpha d) - \frac{\mu_2}{\mu_1} k}{\alpha - \frac{\mu_2}{\mu_1} k \cdot \tanh(\alpha d)} + \frac{\mu_2}{\mu_1} k + \frac{\alpha_d \mu_v}{\tanh(\alpha_d d)} = 0, & (\text{type-2}), \\ \frac{\alpha}{\tanh(\alpha d)} + \frac{\mu_2}{\mu_1} k + \alpha_d \mu_v \cdot \tanh(\alpha_d d) = 0, & (\text{type-3}), \\ \alpha \cdot \frac{\tanh(\alpha d) - \frac{\mu_2}{\mu_1} k}{\alpha - \frac{\mu_2}{\mu_1} k \cdot \tanh(\alpha d)} + \frac{\mu_2}{\mu_1} k + \alpha_d \mu_v \cdot \tanh(\alpha_d d) = 0, & (\text{type-4}), \end{cases} \quad (1)$$

$$\mu_1 = 1 + \frac{\omega_m(\omega_0 - i\nu\omega)}{(\omega_0 - i\nu\omega)^2 - \omega^2}, \quad \mu_2 = \frac{\omega_m\omega}{(\omega_0 - i\nu\omega)^2 - \omega^2}, \quad (2)$$

where  $\nu$ ,  $\omega_0$  ( $=\gamma\mu_0 H_0$ , where  $\gamma$  is the gyromagnetic ratio), and  $\omega_m$  are the damping factor, the precession angular frequency, and the characteristic circular frequency, respectively.<sup>29,30</sup>  $\alpha$  and  $\alpha_d$  denote the attenuation coefficients of the EM wave in the YIG and air layers, respectively.  $d$  represents the thickness of the air and YIG layers.  $\mu_v = \sqrt{\mu_1 - \mu_2^2/\mu_1}$  defines the Voigt permeability. Utilizing Eqs. (1)–(4), we present the dispersion diagram of Surface Magneto-Plasmons (SMPs) in Figs. 1(b)–1(e). Several Asymptotic Frequencies

(AFs) are observed in the dispersion curves, with variations depending on the type of waveguide. In type-1 and type-3 waveguides, the AFs ( $\omega_{sp}$ ) are consistent with  $\omega_{sp}^+ = \omega_0 + \omega_m$  as  $k \rightarrow +\infty$  and  $\omega_{sp}^- = \omega_0 + 0.5\omega_m$  as  $k \rightarrow -\infty$ . When the lower boundary is replaced by a Perfect Magnetic Conductor (PMC) wall, an additional surface band emerges due to the interaction between the PMC-YIG and air-YIG surfaces. The dispersion equation for SMPs on the PMC-YIG interface can be derived from Eq. (1) as  $k = \sqrt{\epsilon_m \mu_1} k_0$  ( $k_0 = \omega/c$ ), resulting in an AF of  $\omega_{sp}^{++} = \omega_0$ . Notably, a portion of the higher branch of red curves in Figs. 1(b) and 1(d) vanishes in type-2 and type-4 waveguides [see Figs. 1(c) and 1(e)], attributed to the absence of the PEC-YIG interface supporting those SMPs.<sup>26</sup>

Additionally, as shown in Fig. 1, INZ modes with  $k=0$  exist in type-1 and type-2 waveguides. Particularly, a unique INZ mode [indicated by the upper green circle in Fig. 1(c)] is observed in the lossless case ( $\nu=0$ ) when  $k=0$  and  $\omega = \omega_s$  ( $= \sqrt{\omega_0(\omega_0 + \omega_m)}$ ). This unique INZ mode has a specific frequency that can be tailored by adjusting the EMF ( $\omega_0$ ). This finding is noteworthy since numerous reported INZ materials operate solely at specific, discontinuous frequencies, even with complex manufacturing processes.<sup>31,32</sup> Figure 2(a) illustrates the relationship between the INZ frequency ( $\omega_{INZ} = \omega_s$ ) and  $\omega_0$ . With an increase in the EMF, the INZ frequency also rises. Importantly, Fig. 2(a) shows a continuous range of INZ frequencies from near zero to  $1.5\omega_m$ . The robustness of these INZ modes was confirmed through simulations. As shown in Fig. 2(b), we designed a composite structure with two type-2 waveguides, placing the source on the right YIG layer to excite left-going non-INZ modes. The excited wave propagated from right to left, and upon encountering the left waveguide, it coupled to the INZ wave with near-zero-phase shift due to the “super-coupling” effect, similar to that observed in ENZ systems. The INZ wave clearly bypassed the imperfection, demonstrating perfect one-way propagation characteristics. Thus, the material’s loss had minimal impact on the INZ modes.

In addition, Fig. 1 illustrates two additional INZ modes, one in the type-1 waveguide [green circle in Fig. 1(b)] and another one in the type-2 waveguide [lower green circle in Fig. 1(c)]. These INZ modes are also tunable by modifying the EMF, akin to the aforementioned INZ mode. To assess the robustness of these INZ modes, we conducted further simulations as shown in Figs. 2(c)–2(f). We introduced imperfections (air holes) into the structures and applied two working frequencies in both type-1 and type-2 structures to compare the behavior of regular SMPs and INZ modes. The simulations demonstrated that both the one-way SMPs and INZ modes can bypass the air hole without reflection. As demonstrated in Fig. 2, the alteration of the lower boundary can invert transmission direction of the one-way modes. Yet, the one-way bands depicted in Figs. 1(a) and 1(b) typically do not overlap. With a PEC bottom boundary, the one-way band extends from  $\omega_m$  to  $1.5\omega_m$ , allowing only forward (+x) one-way waves to transmit. Conversely, replacing the bottom boundary with PMC supports only backward (−x) one-way waves with  $\omega < \omega_m$  in the waveguide. Thus, it is notable that our proposed configurations hold promise for manipulating signal transmission behavior, a crucial aspect in all-optical communication.

We also performed simulations in bent one-way waveguides [depicted in Figs. 2(d) and 2(f)] to assess the robustness of the modes under more stringent conditions. The results showed that both the one-way SMPs and INZ modes are robust under such conditions.

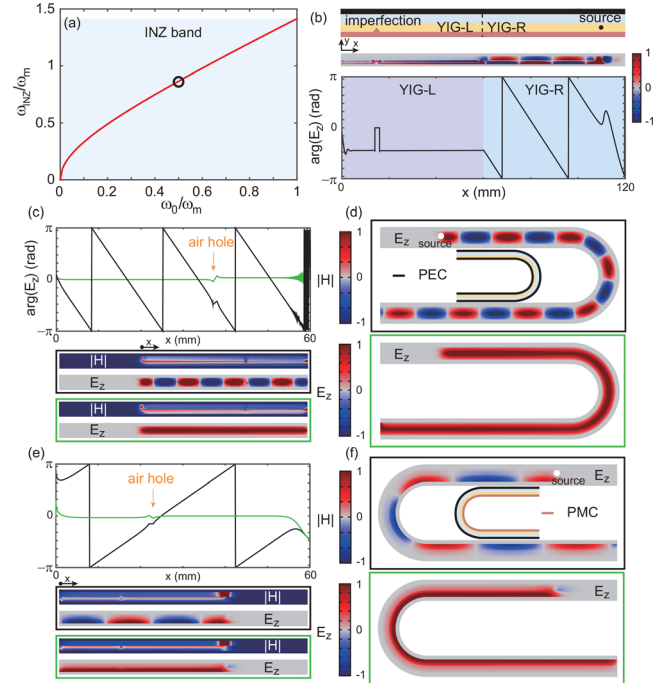


**FIG. 2.** (a) Frequency of the INZ mode ( $\omega_{INZ} = \omega_s$ ) as a function of  $\omega_0$ . (b) Verification of the robustness of INZ modes for  $\omega_0 = 0.5\omega_m$  [indicated by the black circle in (a)]. An imperfection with the height  $\Delta h = 1$  mm was introduced on the PMC-YIG interface. The joint structure used for simulation is shown in the first panel of (b), which consists of two parts of the type-2 waveguide made of YIG with different values of  $\omega_0$ . Specifically,  $\omega_0 = 0.5\omega_m$  was set for YIG-L, and  $\omega_0 = 0.4\omega_m$  was set for YIG-R.  $\omega = 0.86\omega_m$ ,  $\nu = 0.001$ ,  $\lambda_0 = (1/0.86)\lambda_m$ , and  $d = 0.03\lambda_m = 0.0248\lambda_0$ . (c)–(f) Simulation results for (c) and (d) type-1 and (e) and (f) type-2 one-way waveguides. (c) and (e) The lines represent the phase angle of  $E_z$  along the air-YIG interface (c) from the source to the end, and (e) from the end to the source. Air holes with a radius of  $r = 0.5$  mm were set on the air-YIG interface. The working frequencies in the simulations are marked by green (INZ frequencies) and black (reference frequencies) circles in Figs. 1(b) and 1(c), respectively. The INZ frequencies are  $\omega = 1.18\omega_m$  ( $d = 0.0354\lambda_0$ ) and  $\omega = 0.709\omega_m$  ( $d \approx 0.0213\lambda_0$ ), while the reference frequencies are  $\omega = 1.05\omega_m$  ( $d = 0.0315\lambda_0$ ) and  $\omega = 0.6\omega_m$  ( $d = 0.018\lambda_0$ ). Simulations for INZ frequencies are indicated by green lines or green rectangular boxes. The parameters used in the simulations are  $d = 0.03\lambda_m$  and  $\nu = 0.001$ .

It is noteworthy that the one-way INZ modes in all waveguide types are transverse electric (TE) modes. Unlike regular ENZ modes, the group velocity of this type of INZ modes is not near-zero.<sup>33</sup> Therefore, our proposed INZ modes resemble doped ENZ modes, exhibiting EMNZ response exclusively to TE waves.<sup>16</sup>

Variations in the EMF lead to changes in the AFs and dispersion curves, thereby altering the frequencies of the INZs in both type-1 and type-2 waveguides. Figures 3(a) and 3(c) illustrate the relationship between the EMF and the INZ frequencies analyzed in Fig. 2. Remarkably, the INZ frequency is “predictable” for both configurations. Even more exciting is our finding of a nearly linear relationship between  $\omega_0$  and  $\omega_{INZ}$  in type-1 waveguides, as depicted in Fig. 3(a). The equation for this relationship can be expressed as

$$\omega_{INZ} = 0.955\omega_0 + 0.702\omega_m. \quad (3)$$



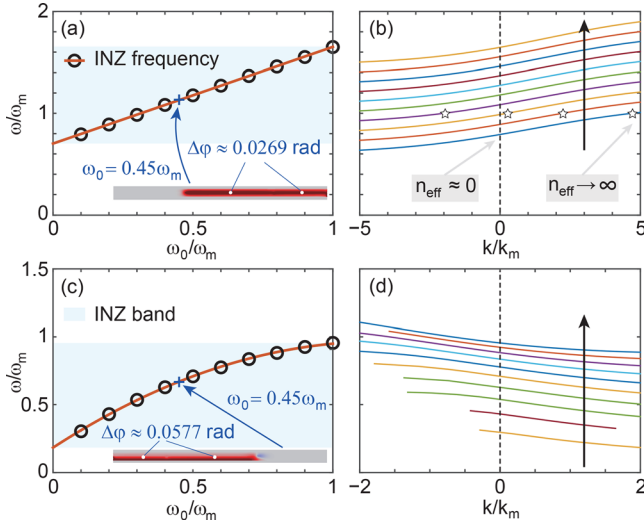


**FIG. 3.** INZ frequencies as a function of  $\omega_0$  in (a) type-1 and (c) type-2 waveguides. The dispersion diagrams in (b) and (d) show a zoom-in view of the INZ modes when  $\omega_0$  is gradually increased from  $0.1\omega_m$  to  $\omega_m$ , as indicated by the black arrows. The stars in (c) represent the modes with  $\omega = \omega_m$ , and the effective index  $n_{\text{eff}} = ck/\omega$  experiences a transition from extremely small values (near the INZ region, marked by the black vertical line) to extremely large values (near the AF region).

Using Eq. (3), one can predict the INZ frequency conveniently for a specific EMF. For example, when  $\omega_0 = 0.45\omega_m$ , Eq. (3) yields  $\omega_{\text{INZ}} \approx 1.132\omega_m$ . Simulation results [inset of Fig. 3(a)] confirm nearly constant electric-field intensity along the propagation direction for  $\omega = 1.132\omega_m$  and  $\omega_0 = 0.45\omega_m$ . Specifically, the phase shift  $\Delta\phi$  is approximately 0.0269 radians after propagating a length of 20 mm, corresponding to about  $0.377\lambda_0$ . Thus, this tunable INZ, predictable with the EMF, accurately represents a linear tunable INZ system. Figure 3(b) illustrates variations in dispersion curves near the INZ modes as  $\omega_0$  changes from  $0.1\omega_m$  (bottom line) to  $\omega_m$  (top line), with the shape and slope of the dispersion curve remaining almost constant. Importantly, in type-1 waveguides, the effective index ( $n_{\text{eff}}$ ) of the SMP can be tuned over a wide range, from near zero (around the INZ frequency) to infinity (around the AF). This adjustable  $n_{\text{eff}}$  is crucial for coupling or communicating between waveguides.

The relationship between  $\omega_{\text{INZ}}$  and  $\omega_0$  for the type-2 structure is shown in Figs. 3(c) and 3(d). For this structure, the equation relating INZ and  $\omega_0$  can be expressed as

$$\omega_{\text{INZ}} = 0.572\omega_0^2 + 1.340\omega_0 + 0.182\omega_m, \quad (4)$$

when  $\omega_0 = 0.45\omega_m$ , Eq. (4) gives  $\omega_{\text{INZ}} \approx 0.669\omega_m$ , and the simulation results for these parameters are shown in the inset of Fig. 3(c), where a near-zero-phase shift is observed as well. The phase shift  $\Delta\phi$  is approximately 0.0577 radians after propagation through a length of 20 mm, which corresponds to approximately  $0.223\lambda_0$ .

The all-optical phase modulator is a pivotal component among all-optical devices, which can be constructed employing configurations such as the Mach-Zehnder interferometer.<sup>34,35</sup> Designing phase modulators with the INZ structures is promising because it preserves the majority of phase information in the EM signal. However, applying

INZ modes in flexible and broadband phase modulation remains challenging due to potential reflections and narrow bandwidth limitations.<sup>36</sup> We note here that the formed bands are robust against dissipative losses,<sup>37,38</sup> and that our magneto-optical structures are also amenable to a plethora of further (e.g., nonlinear<sup>39,40</sup>) effects, allowing potentially for high-speed modulation.<sup>41</sup>

In what follows, we demonstrate that a two- or three-part broadband phase modulator can flexibly modulate the INZ mode and outgoing phase by designing the EMFs. Figure 4(f) illustrates a three-part composite structure with varying EMFs. The EMF in the first part is set to a specific value ( $\omega_0 = 0.5\omega_m$ ) to excite a unidirectional SMP. In the second segment, the EMF is assumed to gradually decrease according to  $\omega_0 = 0.5\omega_m - (0.5 - 0.312)\omega_m/L_1 \times (x - L_0)$ . According to Eq. (3), the EMF in the third part is set to a specific value ( $\omega_0 = 0.312\omega_m$ ) to facilitate the coupling of the incoming EM wave into an INZ mode. As depicted in Figs. 4(b)–4(e), the excited SMP transfers unidirectionally and gradually couple into an INZ mode with an effective wavelength that increases. Further details are presented in Fig. 4(a), where the orange line represents the phase oscillation of  $E_z$  along the air-YIG interface from the source location to the end. The smoothness of the orange line suggests that by modulating the value of  $L_1$ , one should theoretically obtain a continuously varying output phase, i.e., the value at point A. Alternatively, one could simplify the structure by removing the second part. Despite the experimental challenges posed by realizing precisely abrupt EMF changes, the theoretical exploration of the two-part modulator retains research significance. As illustrated by the blue lines in Figs. 4(a) and 4(g), with  $L_1 = 0$ , the incident wave can couple to an INZ mode in the terminal section via one-way propagation, inducing a minor phase shift near the junction. Consequently, the output phase can be controlled by varying  $L_0$ .

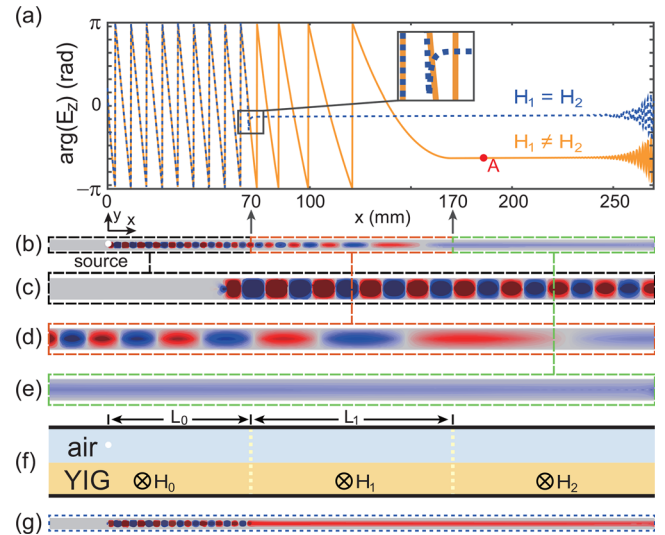


**FIG. 4.** (a)–(e) Simulation results for phase modulation as  $\omega = \omega_m$ , and the EMFs in three parts are  $H_0$ ,  $H_1$ , and  $H_2$ , while the corresponding  $\omega_0$  is  $0.5\omega_m$ ,  $[0.5 - (0.5 - 0.312)/L_1 \times (x - L_0)]\omega_m$ , and  $0.312\omega_m$ , respectively. (f) The schematic diagram of the three-part phase modulator. (g) Simulation result of two-part phase modulator where  $H_1 = H_2$ .  $\omega = \omega_m$ ,  $L_0 = 70$  mm,  $L_1 = 100$  mm, and the other parameters are the same as those in Fig. 2.

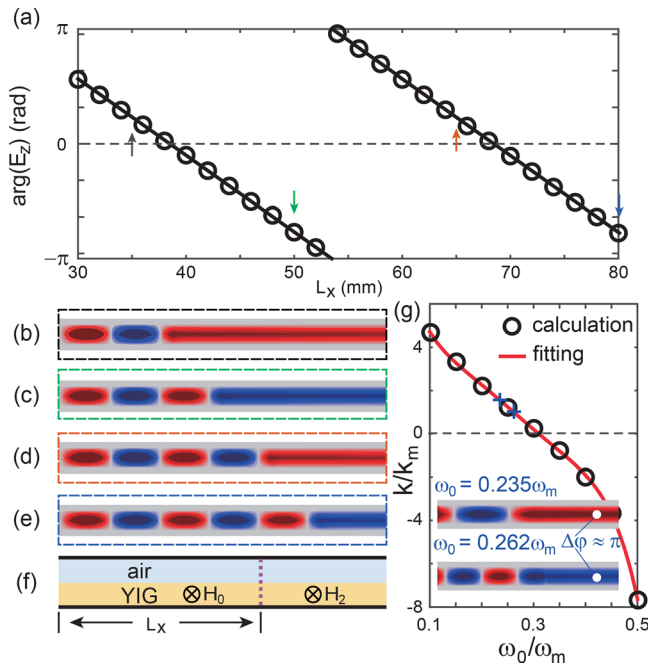


**FIG. 5.** (a) Achieving phase shift from  $-\pi$  to  $\pi$  by modifying  $L_x$ . (b)–(e) Simulation results for phase modulation as  $\omega = \omega_m$  for different  $L_x$  [indicated by arrows in (a)]. (f) The schematic diagram of the two-part phase modulator. (g) Phase velocity ( $k$ ) as a function of  $\omega_0$  in the type-1 structure. The inset illustrates an approximately  $\pi$  phase shift in the two-part phase modulator for  $L_x = 60$  mm under two different EMFs ( $H_0$ ).

In the two-part joint structure shown in Fig. 5(f), different EMFs are applied to the waveguides, specifically  $\omega_0 = 0.5\omega_m$  for the first and  $\omega_0 = 0.312\omega_m$  for the second. Based on our previous analysis of the three-part joint structure, we expect that the output phase angle will be affected by the length of the first part structure ( $L_x$ ). Figures 5(b)–5(e) demonstrate the electric-field distribution for different values of  $L_x$  [indicated by arrows in Fig. 5(a)], showing that the output  $E_z$  propagates in the second part without a phase shift, while the output phase varies. Figure 5(a) shows the correlation between  $L_x$  and the output phase angle of  $E_z$ , clearly demonstrating phase modulation ranging from  $-\pi$  to  $\pi$  through  $L_x$  adjustment. Similarly, phase modulation can also be achieved in the two-part system by adjusting the first EMF. Figure 5(g) illustrates that larger  $\omega_0$  consistently leads to smaller  $k$ . Based on the fitting curve, a two-part structure with  $L_x = \lambda_m = 60$  mm was designed. In this scenario,  $\Delta k \approx 0.5k_m$  as  $\omega_0$  changes from  $0.262\omega_m$  to  $0.235\omega_m$ . An almost  $\pi$  ( $= \Delta k \times L_x$ ) phase shift is observed in this system, as depicted in the inset.

In conclusion, we have introduced two deep-subwavelength ( $\sim 0.01\lambda_0$ ) MO one-way waveguides and identified three predictable and precisely controllable one-way INZ modes: INZ modes with  $\omega_{\text{INZ}} = \sqrt{\omega_0(\omega_0 + \omega_m)}$ , linearly tunable INZ modes, and INZ modes at the PMC-YIG boundary. Through careful design of the EMF in the waveguide, we can modulate the effective index of the EM wave and potentially convert the wave into an INZ mode. The predictable INZ modes offer significant advantages over other INZ modes in

existing systems, such as ENZ metalenses.<sup>8</sup> Contrary to other INZ modes, our proposed INZ modes exhibit tunable behavior across a continuous and broad band eliminating the need for any system configuration alterations. Instead, tunable behavior is achieved solely through the adjustment of EMF. Furthermore, the use of a two- or three-part structure enables precise control of the phase modulation of the outgoing EM wave through EMF engineering, thereby realizing an all-optical phase modulator with a phase shift ranging from  $-\pi$  to  $\pi$ . These findings hold the potential to drive advancements in diverse fields such as all-optical/quantum communication and computing.

This work was supported by the National Natural Science Foundation of Sichuan Province (No. 2023NSFSC1309), the Program of Luzhou Science and Technology Bureau (No. 2023JYJ046), the Scientific Research Projects of China Medical Education Association (No. 2022KTM035), Sichuan Province Science and Technology Support Program (No. 2022YFS0616), and the open fund of Luzhou Key Laboratory of Intelligent Control and Applications Technology of Electronic Devices. (No. ZK202210). J.X. and Y.L. acknowledge the support of the Innovation Laboratory of Advanced Medical Material & Physical Diagnosis and Treatment Technology. K.L.T. was supported by the General Secretariat for Research and Technology (GSRT) and the Hellenic Foundation for Research and Innovation (HFRI) under Grant No. 4509.

## AUTHOR DECLARATIONS

### Conflict of Interest

The authors have no conflicts to disclose.

## Author Contributions

**Panpan He:** Visualization (equal); Writing – original draft (equal). **Yun Shen:** Writing – review & editing (equal). **Sanshui Xiao:** Writing – review & editing (equal). **Lujun Hong:** Writing – review & editing (equal). **Yun You:** Writing – review & editing (equal). **Kosmas L. Tsakmakidis:** Conceptualization (equal); Writing – review & editing (equal). **Yamei Luo:** Supervision (equal); Writing – review & editing (equal). **Jie Xu:** Conceptualization (equal); Supervision (equal); Writing – review & editing (equal).

## DATA AVAILABILITY

The data that support the findings of this study are available from the corresponding authors upon reasonable request.

## REFERENCES

- R. W. Ziolkowski, “Propagation in and scattering from a matched metamaterial having a zero index of refraction,” *Phys. Rev. E* **70**, 046608 (2004).
- I. Liberal and N. Engheta, “The rise of near-zero-index technologies,” *Science* **358**, 1540–1541 (2017).
- X. Niu, X. Hu, S. Chu, and Q. Gong, “Epsilon-near-zero photonics: A new platform for integrated devices,” *Adv. Opt. Mater.* **6**, 1701292 (2018).
- S. Zhong and S. He, “Ultrathin and lightweight microwave absorbers made of mu-near-zero metamaterials,” *Sci. Rep.* **3**, 2083 (2013).
- J. S. Marcos, M. G. Silveirinha, and N. Engheta, “ $\mu$ -near-zero supercoupling,” *Phys. Rev. B* **91**, 195112 (2015).
- A. M. Mahmoud and N. Engheta, “Wave-matter interactions in epsilon-and-mu-near-zero structures,” *Nat. Commun.* **5**, 5638 (2014).

- <sup>7</sup>I. Liberal and N. Engheta, "Zero-index structures as an alternative platform for quantum optics," *Proc. Natl. Acad. Sci. U. S. A.* **114**, 822–827 (2017).
- <sup>8</sup>V. Pacheco-Peña, N. Engheta, S. Kuznetsov, A. Gentslev, and M. Beruete, "Experimental realization of an epsilon-near-zero graded-index metalens at terahertz frequencies," *Phys. Rev. Appl.* **8**, 034036 (2017).
- <sup>9</sup>E. J. R. Vesseur, T. Coenen, H. Caglayan, N. Engheta, and A. Polman, "Experimental verification of  $n = 0$  structures for visible light," *Phys. Rev. Lett.* **110**, 013902 (2013).
- <sup>10</sup>R. Maas, J. Parsons, N. Engheta, and A. Polman, "Experimental realization of an epsilon-near-zero metamaterial at visible wavelengths," *Nat. Photonics* **7**, 907–912 (2013).
- <sup>11</sup>T. Li and J. B. Khurgin, "Hyperbolic metamaterials: Beyond the effective medium theory," *Optica* **3**, 1388–1396 (2016).
- <sup>12</sup>V. Caligiuri, M. Palei, G. Biffi, S. Artyukhin, and R. Krahne, "A semi-classical view on epsilon-near-zero resonant tunneling modes in metal/insulator/metal nanocavities," *Nano Lett.* **19**, 3151–3160 (2019).
- <sup>13</sup>X. Huang, Y. Lai, Z. H. Hang, H. Zheng, and C. T. Chan, "Dirac cones induced by accidental degeneracy in photonic crystals and zero-refractive-index materials," *Nat. Mater.* **10**, 582–586 (2011).
- <sup>14</sup>P. Moitra, Y. Yang, Z. Anderson, I. I. Kravchenko, D. P. Briggs, and J. Valentine, "Realization of an all-dielectric zero-index optical metamaterial," *Nat. Photonics* **7**, 791–795 (2013).
- <sup>15</sup>D. I. Vulis, O. Reshef, P. Camayd-Muñoz, and E. Mazur, "Manipulating the flow of light using Dirac-cone zero-index metamaterials," *Rep. Prog. Phys.* **82**, 012001 (2019).
- <sup>16</sup>Y. Li, C. T. Chan, and E. Mazur, "Dirac-like cone-based electromagnetic zero-index metamaterials," *Light* **10**, 203 (2021).
- <sup>17</sup>Z. Zhou, Y. Li, H. Li, W. Sun, I. Liberal, and N. Engheta, "Substrate-integrated photonic doping for near-zero-index devices," *Nat. Commun.* **10**, 4132 (2019).
- <sup>18</sup>M. Wang, R.-Y. Zhang, L. Zhang, D. Wang, Q. Guo, Z.-Q. Zhang, and C. T. Chan, "Topological one-way large-area waveguide states in magnetic photonic crystals," *Phys. Rev. Lett.* **126**, 067401 (2021).
- <sup>19</sup>X. Yu, J. Chen, Z.-Y. Li, and W. Liang, "Topological large-area one-way transmission in pseudospin-field-dependent waveguides using magneto-optical photonic crystals," *Photonics Res.* **11**, 1105–1112 (2023).
- <sup>20</sup>T. Liu, N. Kobayashi, K. Ikeda, Y. Ota, and S. Iwamoto, "Topological band gaps enlarged in epsilon-near-zero magneto-optical photonic crystals," *ACS Photonics* **9**, 1621–1626 (2022).
- <sup>21</sup>J. Xu, P. He, D. Feng, K. Yong, L. Hong, Y. Shen, and Y. Zhou, "Slow wave and truly rainbow trapping in a one-way terahertz waveguide," *Opt. Express* **29**, 11328–11341 (2021).
- <sup>22</sup>Z. Wang, Y. Chong, J. D. Joannopoulos, and M. Soljačić, "Reflection-free one-way edge modes in a gyromagnetic photonic crystal," *Phys. Rev. Lett.* **100**, 013905 (2008).
- <sup>23</sup>G. Tang, Y. Huang, J. Chen, Z.-Y. Li, and W. Liang, "Controllable one-way add-drop filter based on magneto-optical photonic crystal with ring resonator and microcavities," *Opt. Express* **30**, 28762–28773 (2022).
- <sup>24</sup>L. Liu and Y. Wang, "Unidirectional mode interference in magneto-optical photonic heterostructure," *Opt. Laser Technol.* **161**, 109224 (2023).
- <sup>25</sup>Y. Zhou, P. He, S. Xiao, F. Kang, L. Hong, Y. Shen, Y. Luo, and J. Xu, "Realization of tunable index-near-zero modes in nonreciprocal magneto-optical heterostructures," *Opt. Express* **30**, 27259–27272 (2022).
- <sup>26</sup>Q. Shen, L. Shen, W. Min, J. Xu, C. Wu, X. Deng, and S. Xiao, "Trapping a magnetic rainbow by using a one-way magnetostatic-like mode," *Opt. Mater. Express* **9**, 4399 (2019).
- <sup>27</sup>C. A. Balanis, *Advanced Engineering Electromagnetics* (John Wiley & Sons, 2012).
- <sup>28</sup>Y. Huang, L.-S. Wu, M. Tang, and J. Mao, "Design of a beam reconfigurable THz antenna with graphene-based switchable high-impedance surface," *IEEE Trans. Nanotechnol.* **11**, 836–842 (2012).
- <sup>29</sup>D. M. Pozar, *Microwave Engineering* (John Wiley & Sons, 2011).
- <sup>30</sup>G.-G. Liu, Z. Gao, Q. Wang, X. Xi, Y.-H. Hu, M. Wang, C. Liu, X. Lin, L. Deng, S. A. Yang, P. Zhou, Y. Yang, Y. Chong, and B. Zhang, "Topological Chern vectors in three-dimensional photonic crystals," *Nature* **609**, 925–930 (2022).
- <sup>31</sup>N. Kinsey, C. DeVault, A. Boltasseva, and V. M. Shalae, "Near-zero-index materials for photonics," *Nat. Rev. Mater.* **4**, 742–760 (2019).
- <sup>32</sup>L. Vertchenko, C. DeVault, R. Malureanu, E. Mazur, and A. Lavrinenko, "Near-zero index photonic crystals with directive bound states in the continuum," *Laser Photonics Rev.* **15**, 2000559 (2021).
- <sup>33</sup>M. H. Javani and M. I. Stockman, "Real and imaginary properties of epsilon-near-zero materials," *Phys. Rev. Lett.* **117**, 107404 (2016).
- <sup>34</sup>C. Sturm, D. Tanese, H. Nguyen, H. Flayac, E. Galopin, A. Lemaître, I. Sagnes, D. Solnyshkov, A. Amo, G. Malpuech, and J. Bloch, "All-optical phase modulation in a cavity-polariton Mach-Zehnder interferometer," *Nat. Commun.* **5**, 3278 (2014).
- <sup>35</sup>S. Yu, X. Wu, K. Chen, B. Chen, X. Guo, D. Dai, L. Tong, W. Liu, and Y. R. Shen, "All-optical graphene modulator based on optical Kerr phase shift," *Optica* **3**, 541–544 (2016).
- <sup>36</sup>I. C. Reines, M. G. Wood, T. S. Luk, D. K. Serkland, and S. Campione, "Compact epsilon-near-zero silicon photonic phase modulators," *Opt. Express* **26**, 21594 (2018).
- <sup>37</sup>K. L. Tsakmakidis, A. D. Boardman, and O. Hess, "Tsakmakidis *et al.* reply," *Nature* **455**, E11–E12 (2008).
- <sup>38</sup>E. I. Kirby, J. M. Hamm, T. W. Pickering, K. L. Tsakmakidis, and O. Hess, "Evanescent gain for slow and stopped light in negative refractive index heterostructures," *Phys. Rev. B* **84**, 041103 (2011).
- <sup>39</sup>E. Almpianis, G. P. Zouros, P. A. Pantazopoulos, K. L. Tsakmakidis, N. Papanikolaou, and N. Stefanou, "Spherical optomagnonic microresonators: Triple-resonant photon transitions between Zeeman-split Mie modes," *Phys. Rev. B* **101**, 054412 (2020).
- <sup>40</sup>P. A. Pantazopoulos, K. L. Tsakmakidis, E. Almpianis, G. P. Zouros, and N. Stefanou, "High-efficiency triple-resonant inelastic light scattering in planar optomagnonic cavities," *New J. Phys.* **21**, 095001 (2019).
- <sup>41</sup>F. Y. Gardes, K. L. Tsakmakidis, D. Thomson, G. T. Reed, G. Z. Mashanovich, O. Hess, and D. Avitabile, "Micrometer size polarisation independent depletion-type photonic modulator in silicon on insulator," *Opt. Express* **15**, 5879–5884 (2007).